# Robust UAV Relative Navigation with DGPS, INS, and Peer-to-Peer Radio Ranging

Jason N. Gross, Yu Gu, *Member, IEEE,* and Matthew Rhudy

***Abstract*—This article considers the fusion of Carrier-Phase Differential GPS (CP-DGPS), peer-to-peer ranging radios, and low-cost Inertial Navigation Systems (INS) for the application of relative navigation of small Unmanned Aerial Vehicles (UAVs) in close formation-flight. A novel sensor fusion algorithm is presented that incorporates locally processed tightly-coupled GPS/INS based absolute navigation solutions from each UAV in a relative navigation filter that estimates the baseline separation using integer-fixed relative CP-DGPS and a set of peer-to-peer ranging radios. The robustness of the dynamic baseline estimation performance under conditions that are typically challenging for CP-DGPS alone, such as a high occurrence of phase breaks, poor satellite visibility/geometry due to extreme UAV attitude, and heightened multipath intensity, amongst others, is evaluated using Monte Carlo simulation trials. The simulation environment developed for this work combines a UAV formation flight control simulator with a GPS constellation simulator, stochastic models of the Inertial Measurement Unit (IMU) sensor errors, and measurement noise of the ranging radios. The sensor fusion is shown to offer improved robustness for 3D relative positioning in terms of 3D Residual Sum of Squares (RSS) accuracy and increased percentage of correctly fixed phase ambiguities. Moreover, baseline estimation performance is significantly improved during periods in which differential carrier phase ambiguities are unsuccessfully fixed.**

***Note to Practitioners*- This paper was motivated by the need to enhance the robustness of CP-DGPS/INS relative navigation. In particular, small UAVs exhibit fast dynamics and are often subjected to large and quickly changing bank angles. This in turn induces missed satellite observations and changes in the phase ambiguity. This paper suggests leveraging the emergence of Ultra Wideband ranging radios to directly observe the baseline separation. In this paper, we outline the details of the algorithm implementation. We then use a simulation to show that adding UWB greatly helps to enhance the robustness of the carrier ambiguity integer-resolving algorithm, which is necessary for improved solution accuracy. This work has extensions to ground vehicles, ocean buoys, and space vehicles. In future work we will experimentally validate results.**

***Index Terms*—Relative Navigation, Multi-Sensor Fusion, Differential GPS/INS, Cooperative UAVs, Cooperative Remote Sensing**

## I. INTRODUCTION

ACCURATE (i.e. centimeter-scale) and robust real-time relative baseline knowledge between multiple Unmanned Aerial Vehicles (UAVs) is an enabling technology that has many potential applications. For example, UAV-based cooperative remote sensing, such as distributed Synthetic Aperture Radar (SAR), would enable light-weight, small, and inexpensive transmit/receive elements to be spread amongst formation flying UAVs to form a single large coherent aperture. This would offer the increased flexibility of multiple baseline configurations (i.e. along or cross-track), the ability to synthesize a larger imaging aperture (i.e. not limited by platform size), and redundancy. However, for this concept to be feasible, the relative navigation solution amongst the UAVs must be precisely known (i.e. fraction of radar wavelength ranging from 1/4th up to 1/100th of the wavelength for stringent applications [1]). Likewise, precise relative navigation would enable autonomous aerial refueling [2], and could lead to aircraft fuel savings and active wind gust suppression when coupled with recent advances in wake-vortex and wind-field modeling [3], [4] and close formation flight control [5].

State-of-the-art relative navigation between aircraft in formation flight is based on Carrier-Phase Differential GPS (CP-DGPS) tightly-coupled with INS and has been demonstrated to offer decimeter-to-centimeter-level relative positioning accuracy between formation flying aircraft. In particular, a system was developed for NASA Dryden's F-18 autonomous formation flight program using commercial off-the-shelf components and was demonstrated to provide real-time 7-cm mean error with 13-cm standard deviation error when compared to post-processed DGPS solutions that incorporated static GPS reference stations [6], [7]. To offer improved performance, researchers have studied the fusion of additional sensors for relative navigation. For example, Wang et al. [8] recently considered the fusion of visual navigation beacons (VizNav), INS, and CP-DGPS. Through a simulation study, they showed improved estimation performance with a hierarchically distributed filter architecture that fused all sources when compared to INS/VizNav or INS/CP-DGPS alone. Centimeter-scale relative positioning has been demonstrated in formation flight.

Recent studies have demonstrated the benefits of fusing Ultra-Wideband (UWB) peer-to-peer pulsed ranging radios to benefit GPS by offering enhanced robustness. For example, MacGougan et al. [9] placed UWB radios at surveyed and static locations to augment the GPS constellation, and experimentally demonstrated better accuracy and an improved ability to fix GPS integer phase biases during both static and kinematic applications, especially during periods of poor satellite geometry. Broshears' further conducted an investigation of the potential for using UWB ranges between two GPS receivers

J. Gross and Y. Gu is with the Department of Mechanical and Aerospace Engineering, West Virginia University, Morgantown, WV, 26506 USA e-mail: Jason.Gross (at) mail.wvu.edu

M. Rhudy is with the Department of Mechanical Engineering at Lafayette College, Easton, PA, 18042 USA

Manuscript received August 1, 2014

to constrain the baseline and assist in reducing the ambiguity resolution search space with the constrained Least-squares AMBiguity Decorrelation Adjustment (LAMBDA) method [10]. The approach showed promise over short baselines, and determined that the bias-fixing algorithm could tolerate up to 4-cm of UWB range error with the constrained LAMBDA approach. With their recent availability as low Size Weight and Power (SWaP) commercially available products [11] UWB radio ranging is an attractive navigation aid for autonomous navigation systems [12] such as small UAVs in formation flight.

The work described in this article leverages the recent insight of using UWB ranging as an aid to CP-DGPS/INS to offer an accurate and robust 3D relative navigation solution for UAV close formation flight. The contribution of this work is that a novel DGPS/INS/UWB fusion algorithm is developed and is assessed for the purpose of offering heightened robustness to commonplace error sources that are known to degrade the performance of ambiguity resolved CP-DGPS. The premise of taking this approach is the fact that integer fixed CP-DGPS/INS systems have already been demonstrated experimentally to offer centimeter-scale relative navigation accuracy [7]. Therefore, the role of fusing additional sensors, and primary need for advancing the state-of-the-art, is to increase *robustness* by enhancing the relative navigation filter's ability to *correctly* and *quickly* fix integers phase ambiguities, despite the presence of challenging conditions. This is especially relevant for implementation on small UAV platforms due to their fast dynamics and extreme-bank angles which often lead to dropped satellite observations, poor satellite geometry, and/or phase breaks.

The rest of this paper is organized as follows. Section II describes the overall fusion architecture and details the algorithm formulations for both absolute and relative navigation. Section III describes the West Virginia University (WVU) Phastball UAV research platform, of which the simulation developed for this work is based around. Section IV details the simulation environment developed for this study and the design of the Monte Carlo study. Section V first presents some intermediate results by stepping through and individual simulation trial and then presents the results of the Monte Carlo study. Finally, Section VI offers a summary and conclusions.

## II. Sensor Fusion Algorithm Formulation

The goal of the algorithm developed in the article is to achieve accurate and robust real-time estimation of the relative 3D navigation vector between two UAVs flying in close formation. The two UAVs are denoted as $UAV_A$ and $UAV_B$. The fusion algorithm architecture is shown in Fig. 1, where three sequential estimation stages are indicated.

In *Stage 1*, the absolute navigation state of each each UAV is estimated locally by each UAV by tightly-coupling INS, GPS psuedo-range, and GPS doppler measurements. During *Stage 2*, the raw carrier-phase GPS observables from $UAV_A$ are communicated to $UAV_B$ in order to provide for the formation of double-differences, a two-way time of flight UWB range measurement between the UAVs is obtained, and

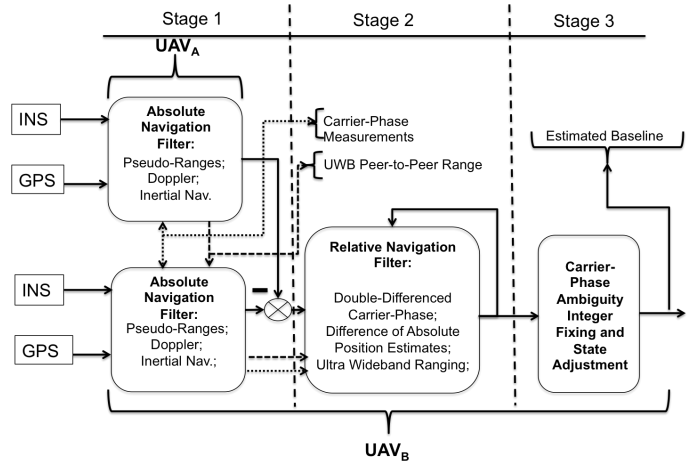


Fig. 1. Architecture for UAV relative baseline estimation. Processing required for one epoch of data.

the difference between the estimated absolute 3D position solutions of $UAV_A$ and $UAV_B$ are subtracted to form an observation in the relative navigation filter. The estimates of *Stage 2* are fed-forward to *Stage 3*, where the phase ambiguity are resolved to integers and the relative navigation vector is adjusted accordingly. The formulation details of each of the three stages is presented next.

### A. Nonlinear Estimator

The sensor fusion algorithms presented in the article are executed using a nonlinear Unscented Kalman Filter (UKF) with sequential measurement updates. For details on implementing the UKF algorithm, the reader is referred to [13]. In this article, we identify the state vector, $x$, measurement vector $z$, output vector, $y$, process model $f$, observation model $h$, as well as, the process noise $Q$ and measurement noise $R$ covariance assumptions used within the implementations presented. These terms are related to each other by considering the Kalman Filter's classic predictor-corrector structure, over discrete-time index $k$. The state prediction is facilitated by a process-model

$$x_{k|k-1} = f(x_{k-1|k-1}, u_k, w_k) \tag{1}$$

and the measurement-update, or state correction, is conducted by using the predicted states in the observation of measurements

$$y_{k|k-1} = h(x_{k|k-1}, d_k, v_k) \tag{2}$$

where the process-noise is assumed to be distributed $w_k \sim N(0, Q)$ and the measurement-noise is assumed to be distributed $v_k \sim N(0, R)$. The process-model $f$ provides for a system input, $u$, and the observation model, $h$ allows for a system input $d$. For the purposes of remaining general, the process-noise, $w_k$ and measurement noise, $v_k$, is incorporated within the respective nonlinear process, Eq. 1, and observation, Eq. 2 models, and is not restricted to be additive noise on the states, $x$, and measurements, $z$, as is in the classic Kalman Filter [14].

### B. Local Absolute Navigation

For the local UAV absolute navigation state estimation, we start with a sensor fusion formulation similar to what we have previously considered which is a 15-state loosely-coupled GPS/INS [14] [15]. However, here adopt a tightly-coupled GPS/INS architecture and therefore also need to include estimation of the GPS receiver's clock bias, clock drift, and a residual wet tropospheric zenith delay, $z_w$. We assume that we are employing a dual-frequency GPS receiver on each UAV, such that ionospheric delays are cancelled to the first order by using the ionosphere-free linear combination [16] . Therefore, the state vector consists of 18-states, including the UAV's local South, West, Down ($L$ for local) position, $\mathrm{r}^L$, and velocity, $\mathrm{v}^L$, the UAV body-axis ($B$ for body) attitude, $[\phi, \theta, \psi]$, time-varying sensor biases of the UAV's Inertial Measurement Unit (IMU), $b(1 \times 6) = b_{a_x,a_y,a_z,p,q,r}$, the GPS receiver's clock bias, $t_b$ and drift rate, $\delta t_b$, and the residual wet zenith delay due to the troposphere , $z_w$.

$$x = \left[\mathrm{r}^L(1\times 3), \mathrm{v}^L(1\times 3), \phi, \theta, \psi, b(1\times 6), t_b, \delta t_b, z_w\right]^T \tag{3}$$

where $\phi$,$\theta$,$\psi$ are the UAV's roll, pitch, and yaw angles respectively.

*1) Prediction:* The state process-model, $f$, for position, velocity and attitude (PVA) consists of integrating the kinematic equations from the previous-estimated navigation state using the IMU sensor measurements as a model input vector, $u = [\mathrm{a}(1\times 3), \omega(1\times 3)]^T$, which are comprised measurements of the UAV's body-axis specific force, $\mathrm{a}_{IMU} = [a_x, a_y, a_z]^T$, and angular rate, $\omega_{IMU} = [p, q, r]^T$. The position vector prediction is simply an integration of the estimated velocity states,

$$f_{\mathrm{r}_l} = \mathrm{r}^l_{k|k-1} = \mathrm{r}^l_{k-1|k-1} + \mathrm{v}^l_{k-1|k-1} T_s \tag{4}$$

where $T_s$ is the filter update rate. The velocity state prediction must consider that the time-varying attitude estimates define a rotating frame, and therefore the IMU specific force measurements must be transformed using a Direction-Cosine-Matrix, $DCM^L_B = DCM(\phi, \theta, \phi)^L_B$, that transforms them from the body-axis to the local frame [17] prior to integrating over time,

$$f_{\mathrm{v}_l} = \mathrm{v}^l_{k|k-1} = \mathrm{v}^l_{k-1|k-1} + \left(DCM^L_{B\,k-1|k-1}\mathrm{a}_k + \mathrm{g}^L\right) T_s \tag{5}$$

where the acceleration due to gravity, $\mathrm{g}^L = \begin{bmatrix}0 & 0 & g\end{bmatrix}^T$, is defined in the local $SWD$ navigation frame. Note that Eq. 5 is assuming that the IMU is measuring the specific force at the aircraft center of gravity, $CG$, which is often not the case. Therefore, it is appropriate to consider the impact of the IMU's lever arm offset from the $CG$, $\mathrm{r}_{IMU/CG}$, as follows,

$$\mathrm{a}_{CG} = \mathrm{a}_{IMU} + \dot{\omega} \times \mathrm{r}_{IMU/CG} + \omega \times \left(\omega \times \mathrm{r}_{IMU/CG}\right) \tag{6}$$

where $\mathrm{r}_{IMU/CG}$ is defined in aircraft body, $B$ coordinates, which is defined as $x$ positive forward, $y$ positive starboard, and $z$ positive down. Next, the attitude is predicted, by integrating $\omega_{IMU}$, concluding the UAV's PVA prediction.

$$\begin{bmatrix}\phi \\ \theta \\ \psi\end{bmatrix}_{k|k-1} = \begin{bmatrix}1 & s(\phi)t(\theta) & c(\phi)t(\theta) \\ 0 & c(\phi) & -s(\phi) \\ 0 & \frac{s(\phi)}{c(\theta)} & \frac{c(\phi)}{c(\theta)}\end{bmatrix} \left[\omega_{IMU}\right]_k \tag{7}$$

Where in Eq. 7 $s(\cdot)$, $c(\cdot)$ and $t(\cdot)$ are abbreviations for sine, cosine and tangent respectively, and the matrix on the right hand side is populated with the estimated attitude states from the previous filter epoch, $k-1|k-1$.

The remaining filter states consist of IMU sensor biases, GPS receiver clock parameters, and the residual wet zenith delay of the troposphere, all of which are predicted using stochastic models. In particular, the IMU sensor biases are modeled using sensor noise density characteristics that are typically reported on the IMU manufacturer's specification sheet, such that a sensor model is given as

$$b_{k|k-1} = b_o + b_{k-1|k-1} + w_{b,k} + w_{w,k} \tag{8}$$

where $b_k$ is the time-varying portion of the IMU bias modeled with random-walk with $w_{b,k}$ defined by the manufacturer's reported 'in-run bias stability'. $w_{w,k}$ is the sensor's wide-band noise density defined by the reported Angular Random Walk (ARW) for the gyros and Velocity Random Walk (VRW) for the accelerometers. $b_o$ is the sensor's initial or 'turn-on' bias, which is modeled as a random constant. The expected $\sigma$ of $b_o$ is also typically reported by the IMU manufacturer and this uncertainty is handled by assigning this value as the sensor bias estimate's *a prior* error-variance when initializing the filter. The GPS clock offset is predicted with the previously estimated drift rate.

$$t_{b\,k|k-1} = t_{b\,k-1|k-1} + (\delta t_{b\,k-1|k-1} + w_{\delta t,k}) T_s + w_{\delta t_b,k} \tag{9}$$

Finally, the residual wet zenith delay is modeled as a slowly time-varying stochastic parameter (i.e. a random-walk rate of ˜10 mm/$\sqrt{hr}$ [18]).

*2) Measurement-Update:* The measurement-update for the absolute navigation filter, updates the predicted states using raw GPS pseudo-range and pseudo-range rate (i.e. doppler) measurements. Because a dual-frequency receiver is used, the ionospheric-free linear combination, $IF$, is used to cancel ionospheric delays to first order [16], [19]. Note, the $IF$ combination is done at the expense of a $\approx$ 3-fold increase in measurement noise [16] which should be handled in the assumed measurement error-covariance. The measurement vector, $z$, consists of $n$, pseudo-range measurements, $\rho_{IF}$, and $n$ pseudo-range-rate measurements, $\dot{\rho}_{IF}$

$$z = \begin{bmatrix}\rho^{1\ldots n}_{IF} & \dot{\rho}^{1\ldots n}_{IF}\end{bmatrix} \tag{10}$$

.

The output-vector, $y$, uses the predicted state to compute the expected observable and forms the filter's Observed-Minus-Computed (OMC), or innovation residuals. The observation function for an individual pseudo-range measurement, $h_\rho$, of satellite, $j$, to a user, $u$, is equal to the predicted geometric range, which is determined from the norm of the predicted user position vector and the satellite's position vector that is provided in the broadcast navigation data. In addition, the additional range attributed to predicted clock bias, $t_b$, times the speed of light, $c$, and residual wet delay of the troposphere in the zenith direction, $z_w$, mapped into a line-of-site delay by the use of an obliquity factor that is provided as a function GPS satellite's elevation angle, $el.$, with respect to the users predicted location, $M(el)$ [16]. To formulate the geometric range, the estimated position vector, $r^l$, must be transformed into the WGS-84 Earth Centered Earth Fixed (ECEF) coordinate system, denoted as $E$, that is used by the GPS broadcast ephemeris, using the transformation approach that is documented in many texts [20].

$$h_\rho = y_\rho = \|\mathrm{r}_u^E - \mathrm{r}_{Sat_j}^E\|_2 + M(el.)z_{w,k|k-1} + ct_{b,k|k-1} + v_\rho \tag{11}$$

The observation function of the pseudo-range rate observations, projects the difference of the predicted velocity vector and the satellite velocity vector to the unit vector between the receiver and the satellite. Additionally, the range-rate attributed to the predicted clock drift-rate is considered. Again, the predicted velocity vector, $v^l$, must be transformed into WGS-84 coordinates. The observation function of the range rate from a satellite, $j$, to user, $u$ is given as

$$h_{\dot\rho} = y_{\dot\rho} = \|\mathrm{v}_u^E - \mathrm{v}_{Sat_j}^E \underline{1}_u^j\|_2 + c\delta t_{bk|k-1} + v_{\dot\rho} \tag{12}$$

where $\underline{1}_u^j$ is the unit vector from user, $_u$ and satellite $j$ that is determined from the predicted position vector, $r_u^E$, and satellite position, $r_{Sat_j}^E$. the pseudo-range rates are from instantaneous doppler measurements, and are effected by phase-breaks. Here, we assume that the change in the tropospheric delay is negligible between epochs [16]. Within this study, the occurrence of a phase break is assumed known *a priori* from a dual-frequency data editing algorithm [21] , and therefore these measurements are skipped over in the measurement-update.

The measurement-error covariance matrix, $R$ is a square $2 \times n$ sized diagonal matrix with the upper-left $n$ diagonal elements, $v_\rho^2$, and the lower-right diagonal elements equal to $v_{\dot\rho}^2$. For this study, $v_\rho = 1m$ was used and $v_{\dot\rho} = 8cm$ are used for nominal values, which are scaled in run-time according to the elevation angle of the particular GPS satellite being modeled for a given observation. In particular, the assumed error-variance is scaled by $\frac{1}{sin(el.)}$. Elevation dependent weighting is a standard approach to deal with model uncertainties associated with the atmospheric delays [22].

### C. Cooperative Relative Navigation Filter

The cooperative relative navigation filter uses the UWB peer-to-peer range measurement as a direct measurement of the baseline distance and a difference of both UAV's local absolution position estimates to augment a local DGPS algorithm for estimating the dynamic 3D relative position vector between the UAVs. The DGPS algorithm uses double-differenced carrier-phase GPS observables.

*1) Prediction:* The state vector for the relative navigation filter, $x$, consists of the 3D relative position vector between $UAV_A$ and $UAV_B$ in an Earth Centered Earth Fixed (ECEF) frame , $\mathrm{r}_{A/B} = \begin{bmatrix}\Delta X & \Delta Y & \Delta Z\end{bmatrix}$, time-varying biases that correct the difference of the two local absolute navigation filter solutions to the estimated relative navigation vector, $\delta\mathrm{r}_{A/B} = \begin{bmatrix}\delta_{\Delta X} & \delta_{\Delta Y} & \delta_{\Delta Z}\end{bmatrix}$, and the phase ambiguities, $N$ on the L1 and L2 double-differenced carrier phase measurements

$$x = \begin{bmatrix}\mathrm{r}_{A/B} & \delta\mathrm{r}_{A/B} & N_{L1}^{i..n} & N_{L2}^{i..n}\end{bmatrix} \tag{13}$$

where the $\delta\mathrm{r}_{A/B}$ states are included to take advantage of the fact that the position estimation errors due un-modeled error-source in the two absolute position navigation filters are time-correlated. For prediction, the 3D relative position vector and its bias with respect to the difference of the two absolute solutions are modeled as random-walk, and the phase ambiguities states are assumed to be random constants, therefore, the prediction model for the 3D navigation vector, $f_{3DRel}$, is of the form

$$\mathrm{r}_{A/B_{k|k-1}} = \mathrm{r}_{A/B_{k-1|k-1}} + w_{3D} \tag{14}$$

$$\delta\mathrm{r}_{A/B_{k|k-1}} = \delta\mathrm{r}_{A/B_{k-1|k-1}} + w_{\delta_{3D}} \tag{15}$$

and the prediction model of the phase biases, $f_\phi$, is

$$N_{k|k-1} = N_{k-1|k-1} \tag{16}$$

where the process-noise is zero. This is the case as long the tracking of a particular satellite and the reference satellite is continuous on both receivers used for the DGPS solution.

Whenever a phase break occurs, a white-noise reset is performed on the impacted double-differenced phase ambiguity estimate. A white-noise reset consists of resetting the estimated phase bias to zero, resetting the estimate variance of the phase bias to a large value (e.g. one second at the speed of light), and zero-ing out the covariances of the phase ambiguity state and all of the other filter states. For the purposes of this article, the occurrence of a phase break is assumed to be known *a priori* through the use of a dual frequency data editing algorithm [21].

*2) Measurement-Update:* For the measurement-update of the relative navigation filter, we first consider the observation model of the undifferenced GPS carrier-phase measurements, which are written as [16]:

$$\phi = \lambda^{-1}[r + I_\phi + T_\phi] + \frac{c}{\lambda}(\delta t_u - \delta t^s) + N + \epsilon_\phi \tag{17}$$

where the carrier-phase, $\phi$, is in units of cycles of the wavelength, $\lambda$, which is in units of meters, $r$ is the geometric range in meters, $I$ is ionospheric delay in meters, $T$ is the tropospheric delay in meters, $c$ is the speed of light in $m/s$, $\delta t$ are clock biases of the user's receiver $u$ and satellite transmitter $S$ in seconds, and $\epsilon$ represents the multipath error with units of meters. Additionally, the unknown number of integer cycles, $N$.

The primary observables for local-area DGPS applications are double-differenced carrier-phase measurements, where, first, two measurements from the same satellite, $j$ are differenced between the two user receivers, denoted as $A$ and $B$, to form single-differenced carrier-phase measurements

$$\Delta\phi_{A,B}^j = \lambda^{-1} r_{A,B}^j + \frac{c}{\lambda}\delta t_{A,B} + N_{A,B}^j + \epsilon_{\phi,A,B}^j \tag{18}$$

where the satellite clock bias errors are eliminated. Furthermore, whenever a short baseline between receivers $A$

and $B$ is assumed, the troposphere and ionosphere delays are also eliminated. In order to further eliminate the error attributed to the combined user's receiver clock biases, $\delta t_{A,B}$, two single-differenced measurements from satellites $j$ and $k$ are subtracted to form double-differenced carrier-phase measurements, which are indicated as $\nabla\Delta\phi_{A,B}^{j,k}$ . Double-differences are often formed by selecting a high-elevation satellite as the reference satellite (indicated in this paper as $k$) and subtracting its single-difference measurement from all other available single-difference measurements. With double-differenced measurements, the only errors that remain are the multipath errors and the ambiguity, which is known to be an integer number of wavelengths of the carrier frequency.

The measurement vector of the relative navigation filter, $z$, consists of $n$ double-differenced phase measurements for each the L1 and L2 frequency, the 3D relative position vector estimated by differencing the two local absolute filter position estimates, $\mathrm{r}^{\Delta_{abs}}_{A/B_{k|k-1}} = \begin{bmatrix}\Delta X & \Delta Y & \Delta Z\end{bmatrix}_{\Delta_{abs}}$, and the UWB peer-to-peer range between the UAVs, $R_{UWB}$.

$$z = \begin{bmatrix}\nabla\Delta\phi_{L1}{}^{i \ldots n,k}_{A,B} & \nabla\Delta\phi_{L2}{}^{i \ldots n,k}_{A,B} & \mathrm{r}^{\Delta_{abs}}_{A/B_{k|k-1}} & R_{UWB}\end{bmatrix} \tag{19}$$

The observation function for an individual double-differenced phase measurement, $h_\phi$, between satellite $j$ and reference satellite $k$ on frequency $f$ (i.e. L1 or L2) is defined as

$$z_\phi = \nabla\Delta\phi_f{}^{j,k}_{A,B} = y_\phi = \begin{bmatrix}-(\underline{1}^j_A - \underline{1}^k_A)^T\end{bmatrix} \mathrm{r}_{A/B_{k|k-1}} + \lambda_f N^j_f + v_\phi \tag{20}$$

where the 3D relative position vector, $\mathrm{r}_{A/B_{k|k-1}}$ , is from the filter prediction step, the phase ambiguity $N^j_f$ is from the filter's prediction step, $\lambda_f$ is the wavelength of the measurement (i.e. L1 or L2), $\underline{1}^j_A$ is the unit vector from receiver $A$ to satellite $j$, and $v_\phi$ is the measurement noise assumed for double-differenced phase observables.The observation function for the 3D estimate relative position vector formed by differencing the two absolute position estimates, $h_{\Delta_{abs}}$, adds the estimated biases to predicted 3D relative position vector and accounts for the measurement noise of the two local absolute position solutions

$$z_{3D_{\Delta_{abs}}} = \mathrm{r}^{\Delta_{abs}}_{A/B_{k|k-1}} = \mathrm{r}_{A/B_{k|k-1}} + \delta\mathrm{r}_{A/B_{k|k-1}} + v_{3D_{\Delta_{abs}}} \tag{21}$$

where, again, the 3D relative position vector is from the filter prediction.

The observation function of the UWB peer-to-peer range, $h_{UWB}$ is the $L_2$ norm of the 3D relative position vector

$$z_{UWB} = R_{UWB} = y_{UWB} = \|\mathrm{r}_{A/B_{k|k-1}}\|_2 + v_{UWB} \tag{22}$$

where the UWB peer-to-peer measurement is used as direct measurement of the baseline separation between the GPS receiver antenna phase center on $UAV_A$ and $UAV_B$ and $v_{UWB}$ is the noise assumed for the UWB measurement. Note that if there is a lever-arm between the GPS antenna and the UWB antenna, it should be accounted for in Equation 22.

The measurement-error covariance matrix assumes 20 cm meter-level errors in the range-only 3D relative navigation solution, $v_{\Delta_{abs}}$, 1 cm-level noise on the double-differenced phase measurements, $v_\phi$, and 10 cm measurement error is assumed for UWB measurement, $v_{UWB}$. Therefore, the measurement-error covariance, $R$, is of the form

$$R = diag(\begin{bmatrix}v^2_{\phi,1} & \ldots & v^2_{\phi,n} & v^2_{\Delta_{abs}} & v^2_{\Delta_{abs}} & v^2_{\Delta_{abs}} & v^2_{UWB}\end{bmatrix} \tag{23}$$

### D. Ambiguity Bias Fixing and State Adjustment

After each measurement update, the UKF estimated phase ambiguities, which do not take advantage of the fact that they are an integer number of wavelengths, are fed to an integer ambiguity resolution algorithm along with their estimated variance-covariance matrix. In particular, the LAMBDA method [23], [24] was used for this implementation. The objective of the LAMBDA method find an Integer Least Squared Solution (ILS) with respect to the estimated float ambiguities, $\hat{N}_\phi$, and corresponding variance-covariance estimate of the phase ambiguities, $P_{\hat{N}_\phi,\hat{N}_\phi}$, by searching a set of integer grid points,$N_\phi$, by minimizing the following relationship over multiple candidate solutions [23]:

$$F(N_\phi) = \left(\hat{N}_\phi - N_\phi\right)^T P^{-1}_{\hat{N}_\phi,\hat{N}_\phi} \left(\hat{N}_\phi - N_\phi\right) \leq \chi^2, N_\phi \in^n \tag{24}$$

where the integer grid search space is defined by the size of $\chi^2$.

With the integer-fixed biases, the 3D relative navigation states are updated accordingly, by assuming that the integer fixing is a deterministic process, using the following equation

$$x^{\text{fix}}_{\text{non}\hat{N}_\phi} = x^{\text{float}}_{\text{non}\hat{N}_\phi} - P_{\text{non}\hat{N}_\phi,\hat{N}_\phi} P_{\hat{N}_\phi,\hat{N}_\phi}(\hat{N}_\phi - N_\phi) \tag{25}$$

where $P$ refers to the estimated variance-covariance matrix for the float solution, which particular sections identified by the subscripts $non\hat{N}_\phi$, which refers to the states that are not phase ambiguities and $\hat{N}_\phi$, which refers to phase ambiguity states. Bias fixing is done in a complimentary manner to the UKF, such that the fixed ambiguities and the associated adjusted relative navigation states are not fed to the next filter step, but are instead saved as a separate estimate.

Not all attempts to fix biases to integer values will be a success in the presence of errors. The specific method employed as in acceptance test of the integer fixed phase ambiguities, is the ratio-test [25]. The ratio-test tests how close the float ambiguity estimates are to the best integer ambiguity estimates when compared to the next best integer ambiguity candidate. The best candidate, $N^{1^{st}}_\phi$, and second best candidate, $N^{2^{nd}}_\phi$ are the two candidates that minimize the quadratic cost function, $F(N_\phi)$ of Equation 24 the most [25]

$$\text{Accept } N^{1st}_\phi \textbf{ iff } \frac{F(N^{1^{st}}_\phi)}{F(N^{2^{nd}}_\phi)} \leq \frac{1}{C} \tag{26}$$

where $C$ is the critical value, which can be derived on-the-fly to allow a fixed failure rate or set to a constant [25].

Smaller values of C will lead to more candidates that fail, but offers a less likely chance of incorrectly accepting a set of incorrect integer ambiguities. A constant value is often used for $C$, although this has been chosen empirically without a rigorous justification [25]. Nonetheless, for this study, $C$ was set to 3 and held constant, as the main purpose of this work is to assess the impact of including the UWB range information.

## III. WVU Phastball UAV

The WVU *Phastball* aircraft was designed to be a modular and low-cost UAV platform that can support a wide range of flight research topics. It uses a custom designed flexible avionics package [26] which will be upgraded to include a ranging radio in order to experimentally validate the results of this simulation study. The *Phastball* design, shown in Figure 2 has a 2.4 meter wingspan and a 2.2 meter total length. The typical takeoff weight is 10.5 Kg with a 3.2 Kg

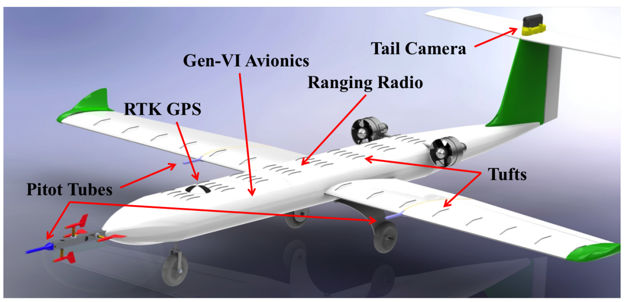


Fig. 2. WVU *Phastball* Research UAV design with main navigation components indicated.

payload capacity. The aircraft is propelled by two brushless electric ducted fans, each providing up to 30 N of static thrust, offering a cruise speed of approximately 30 m/s. A recent close formation flight experiment incorporating two *Phastball* UAVs is shown in Figure 3.

Fig. 3. Summer 2013 *Phastball* close-formation flight.

## IV. Simulation Environment

### A. Overview

The simulation environment developed for this study incorporates a dynamic model of the *Phastball* UAV within Formation Flight simulation environment (WVU-FF-Sim), GPSoft's SatNav 3.04 Matlab Toolbox [27], a stochastic model for IMU sensor noise based on a manufacture's specifications [28], and assumes a normal noise density on the UWB range measurements. The WVU-FF-Sim's dynamic models for the WVU *Phastball* UAV were derived using flight data [29], and the formation controller is based on Nonlinear Dynamic Inversion (NLDI) control laws [30], of which control performance of the simulation has been validated against actual formation flight tests [3]. A bird's eye view of a sample simulated trajectory is shown in the top panel of Figure 4 where the typical baseline separation between the UAVs in this simulation is approximately 30 meters (bottom panel).

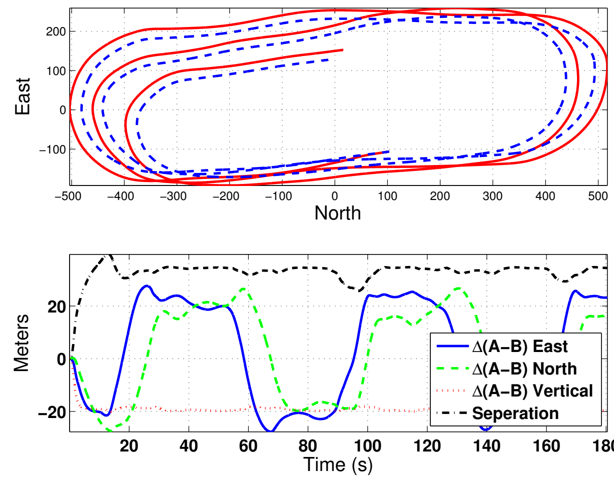


Fig. 4. Simulated truth trajectory for 2 UAV formation flight (top). Baseline separation of formation (bottom).

### B. Model Details

Once reference trajectories for $UAV_A$ and UAV$_B$ are generated from WVU-FF-Sim, the corresponding dual-frequency GPS pseudo-range, carrier-phase and doppler observables are generated using the SatNav 3.04 Matlab Toolbox. To ensure diversity with respect to satellite geometry and modeled atmospheric delays, the origin of the flight is randomly initialized to a new location on Earth for each simulation trial, and a simulation start time (GPS time-of-week) is randomly selected. Furthermore, IMU sensors are modeled with realistic errors and UWB range measurements are developed by polluting the actual baseline magnitude with measurement noise. A summary of all of the models and error-source magnitudes are listed in Table I.

As referenced in Table I, a modification was made in the SatNav-3.04 to allow for the simulation of carrier-phase breaks. To do this, first each phase arc is given a randomly initialized ambiguity. Next, because the chance of a phase-break occurrence goes up with extreme aircraft attitude, a likelihood was assigned to perform a uniform random test any time a UAV was beyond a specific $\phi$ threshold. Furthermore, to model satellite visibility dependent on UAV attitude, the elevation angle of each simulated satellite's line-of-sight vector was transformed into the aircraft body-axis and an assumed mask was applied [34]. To illustrate these models, a sample of

TABLE I
SIMULATED ERROR SOURCES ON SENSOR OBSERVATIONS.

| Error-Source | Model Parameters | Reference/Notes |
|---|---|---|
| **IMU Accelerometers** | Initial-Bias $\sigma = 50mg$ , VRW= $0.2\frac{m/s}{\sqrt{hr}}$ | Analog Devices, Inc. ADIS16405 [28] |
| **IMU Rate Gyroscopes** | Initial-Bias $\sigma = 3\frac{\circ}{s}$, ARW= $2.0\frac{\circ}{\sqrt{hr}}$ | Analog Devices, Inc. ADIS16405 [28] |
| **GPS Thermal Noise** | $\rho \sim \sigma = .32m$, $\phi \sim \sigma = 0.16\lambda m$ | Sat-Nav-3.04 [27] |
| **GPS Multipath** | 1.0 Intensity : $\sigma = 0.4m$, $\tau = 15$min. | Sat-Nav-3.04 [27], Intensity varied randomly. |
| **GPS Tropospheric Delay** | % of error assumed handled by broadcast correction (randomly initialized, see set-up below) | Sat-Nav-3.04 [27], Modified Hopfield algorithm [31] |
| **GPS Ionospheric Delay** | 50% error assumed handled by broadcast correction | Sat-Nav-3.04 [27], Raised half-cosine [32] scaled by FAA WAAS obliquity factor [20] |
| **GPS Receiver Clock Bias** | Initial-Bias $\sigma = 30ns$, $\delta\tau_b = 100\frac{ns}{s}$ | Tuneable |
| **GPS Phase Ambiguity** | Random initialization and phase breaks correlated with UAV attitude | See description in this paper. Varied from 0.5% to 5.0% likelihood |
| **GPS Broadcast Orbits/Clocks** | Orbits $\sigma = 100cm$ Clocks: $\sigma = 2.5ns$ | International GNSS Service [33] |
| **UWB Range Measurement Error** | $\sigma = 10cm$ | Time Domain P410 Radio [11] |

UAV number of satellites in-view, roll angle, $\phi$, and double-difference phase arc on GPS L1, $\nabla\Delta\phi_{L1}$ is shown in Figure 5 .

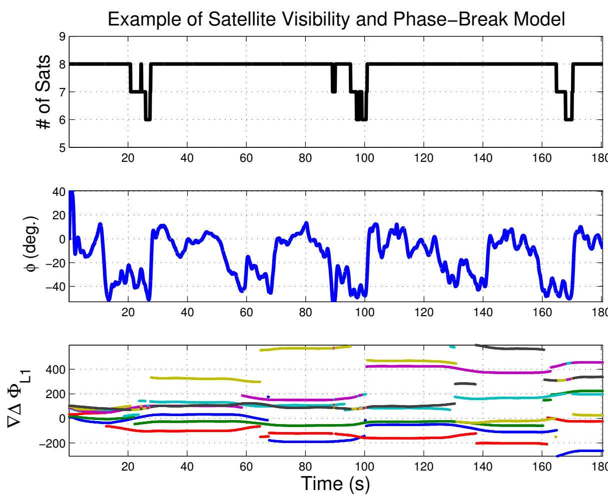


Fig. 5. Simulated satellite visibility (top) and phase-breaks (bottom) taking into account UAV attitude ($\phi$ angle shown in middle for reference).

In Figure 5 in the absence of any phase-breaks, the $\nabla\Delta\phi_{L1}$ would be absent of discontinuities.

### C. Monte Carlo Set-up

Using there error-source models listed in Table I, each Monte Carlo simulation trial was randomly initialized as follows:

- **Break likelihood** $\geq \phi_{\mathbf{thresh}}$: Uniformly selected from 0 to 10%, with $\phi$ threshold of 30°;
- **UWB range noise**: $\sigma$ uniformly selected from 2.5 to 10 cm;
- **IMU Precision**: Noise densities scaled linearly from ADIS-16405 [28] IMU, uniformly selected from 0.5 to 1.5;
- **Troposphere Residual Delay**: Scaled linearly, uniformly selected from 0.1 to 0.9;
- **Multipath Intensity**: Uniformly selected from 0 to 1.

In total 750 trials were run for this study. Each flight was simulated for 180 second duration and GPS, IMU and UWB measurements were generated for fusions at a rate of 10 Hz. For each trial the local absolute navigation filters are run first, and then the relative navigation filters with and without UWB, using the same CP-DGPS and INS measurements.

### D. Ranging Radio System

For this simulation study, the particular UWB ranging radio system considered is Time Domain's P-410 [11], which is shown in Figure 6. For this UWB system, a system trade

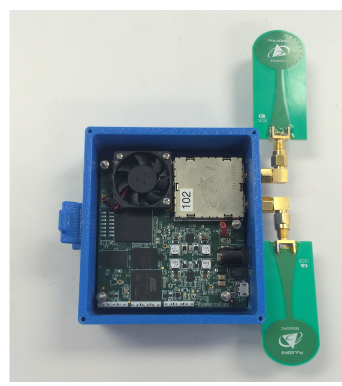

Fig. 6. Time Domain's P-410 UWB Module

was developed and presented in our preliminary work on this topic [35] in terms of maximum measurement range, communications throughput and available update rate. In that study, it was determined that this particular UWB ranging system was capable of providing up to 200 meters of peer-to-peer range measurements at an update rate of 10 Hz, while allowing for up to 256 bytes of communication throughput. To assist the reader when considering UWB integration in their own application, they are referred to [35] , where the models used to make these assessments are detailed.

## V. RESULTS AND DISCUSSION

### A. Example Simulation Trial

To facilitate the discussion of the results, first, some intermediate results from a single simulation trial are provided as an example. The results are from the simulation that is consistent with the satellite visibility and break model plot shown in Figure 5. An example of the local absolute navigation performance for a single UAV is shown in Figure 7.

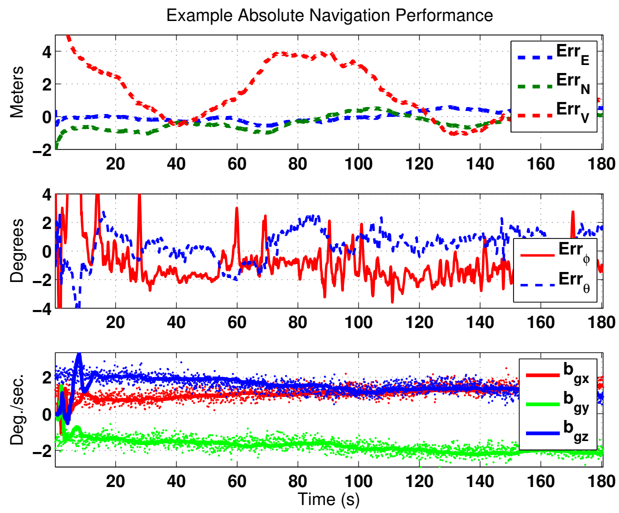


Fig. 7. Example performance of absolute navigation filter. Position error (top). Attitude error (middle). Gyro bias estimate (solid line) vs. simulated gyro bias and noise (dots) (bottom).

For this particular simulation trial, the IMU Errors were scaled to 0.86 with respect to ADIS-16405 specification sheet reported noise densities [28], the likelihood of phase breaks was 4.05% when the UAV was $\geq 30°$, the $\sigma$ of the UWB range error is 7.95 cm, the start time was 1019 seconds in the GPS week, and the origin was 43.16°latitude and 56.31°longitude. As expected the vertical solution has the largest error. The attitude estimation is $\approx 1°$-level accurate, which is consistent with our previous experimental studies [14], [15], and the IMU sensor biases are estimated correctly.

Finally, using the same simulation trial of which one of the absolute navigation performance was shown in Figure 7, the relative baseline estimation performance of the fused DGPS/INS/UWB solution is shown in Figure 8. In Figure 8, the dropped satellites and phase breaks that occur during large aircraft roll angles, as shown in Figure 5, lead to periods in which the ratio test fails and the float solution is accepted. Overall, 68% of the epochs successfully pass the ratio-test. Because of the incorporation of UWB range measurements, the float solution baseline estimation error remains under 10cm for most of the flight.

### B. Monte Carlo Results

Table II summarizes the ambiguity fixed baseline estimation performance with and without the inclusion of the UWB peer-to-peer range measurements for 750 Monte Carlo trials. In this analysis, the primary metric we consider for performance is $3D_{RSS}$.

$$3D_{RSS} = \sqrt{E^2_{X_{RMS}} + E^2_{Y_{RMS}} + E^2_{Z_{RMS}}} \tag{27}$$

In Table II the top 6 rows report statics only calculated using epochs that pass the LAMBDA ratio acceptance test

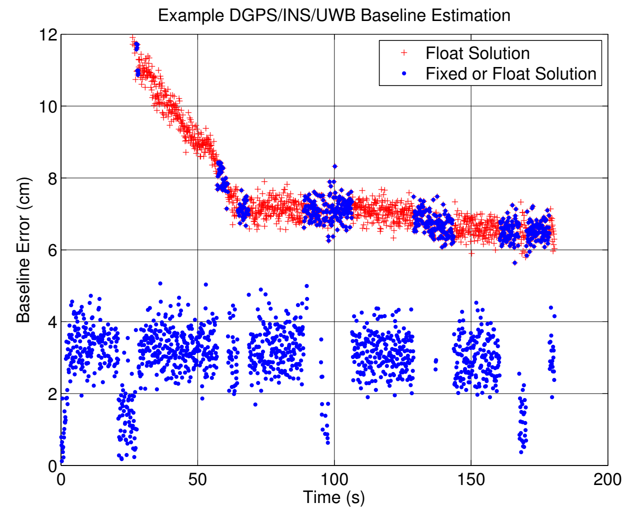


Fig. 8. Example performance of the DGPS/INS/UWB relative navigation filter comparing the float solution to the fixed or float solution. 68% of this epochs were successfully fixed during this simulation trial.

TABLE II
DYNAMIC BASELINE ESTIMATION PERFORMANCE STATISTICS OF THE INTEGER-FIXED EPOCHS, ALONG WITH STATISTICS OF FIXING EFFICIENCY.

| 750 Trials | with UWB | without UWB |
|---|---|---|
| % of Trials with $3D_{RSS}$ $<= 10cm$ | 99.60 | 98.80 |
| Median Fixed $3D_{RSS}$ (cm) | 2.82 | 2.78 |
| Mean Fixed $3D_{RSS}$ (cm) | 5.85 | 477.84 |
| $\sigma$ Fixed $3D_{RSS}$(cm) | 56.55 | 8993.38 |
| Min Fixed $3D_{RSS}$(cm) | 0.43 | 0.43 |
| Max Fixed $3D_{RSS}$ (cm) | 1368.04 | 220509.60 |
| Median % of Epochs Fixed | 58.48 | 27.34 |
| Mean % of Epochs Fixed | 53.92 | 30.89 |
| $\sigma$ % of Epochs Fixed | 32.36 | 24.27 |
| Min % of Epochs Fixed | 0.11 | 0.11 |
| Max % of Epochs Fixed | 100.00 | 100.00 |

criteria. The top row is an indication of the overall reliability of correctly fixing. In particular, 99.6% and 98.8% of the reported fixed solutions have a total $3D_{RSS}$ estimation error of under 10 cm with and without UWB respectively. This indicates, that in these trials all epochs that were fixed, were done so correctly. Further, in a median sense, the fixed solutions with and without UWB are nearly identical. This is consistent with the belief that UWB should not be viewed as a means to improve accuracy, but to improve accuracy of robustness. At first glance it may seem that including UWB range measurements offers little improvement. However, if we consider the remaining 0.4 % for UWB and 1.2% indicated trials in which an epoch was reported fixed for UWB and without UWB respectively, we see that the severity of the incorrectly fixed epochs without UWB ranges is far worse. This is indicated by considering the mean fixed error in row three, which suggests that the trials that have epochs reported incorrectly without UWB are drastically wrong in comparison with UWB ranging included. That is the mean error is skewed two orders of magnitude without UWB, while remaining that same order with UWB. This claim is further substantiated by comparing the $\sigma$'s reported in row four, which show more consistently results when UWB peer-to-peer ranges are includes. Finally, the maximum $3D_{RSS}$ error of the 750 trials is significantly (several orders of magnitude) lower for the filters that use peer-to-peer ranging.

The true benefit of including UWB peer-to-peer ranging becomes more apparent when looking at the improvement with respect to comparing the % of epochs successfully fixed. These metrics are reported in the second half of Table II. Both in a mean and median sense, the inclusion of the UWB range measurements leads to ≈20% more epochs successfully fixed. Because it is less informative to independently consider the estimation performance of fixed solution without also considering the % of epochs that were fixed, we present Table III, which normalizes the fixed $3D_{RSS}$ estimation performance by the % of epochs fixed trial-by-trial. In Table III, the

TABLE III
BASELINE ESTIMATION PERFORMANCE STATISTICS OF FIXED SOLUTION, NORMALIZED BY % OF EPOCHS FIXED.

| 750 Trials | with UWB | without UWB |
|---|---|---|
| **Normalized % of Trials with $3D_{RSS} <= 10cm$** | 99.9 | 45.2 |
| **Normalized Median Fixed $3D_{RSS}$ (cm)** | 5.35 | 10.17 |
| **Normalized Mean Fixed $3D_{RSS}$ (cm)** | 48.53 | 22879.17 |
| **Normalized $\sigma$ Fixed $3D_{RSS}$ (cm)** | 575.02 | 462595.85 |
| **Normalized Min Fixed $3D_{RSS}$ (cm)** | 1.59 | 1.69 |

increased level of robustness by including the peer-to-peer range measurements is much clearer. For instance, even after penalizing $3D_{RSS}$ by fixing efficiency rate, 99.9% of trials still exhibit better than 10 cm performance when the UWB measurements are included. This is more than cut in half for the trials without UWB. Further, now the median statistic is around two-fold better for the UWB case than without UWB, whereas the reported medians were nearly identical in Table II.

Finally, we can draw additional insight if we simply compare $3D_{RSS}$ for all epochs. That is, irrespective of successfully fixing ambiguities. This represents the estimation filters overall *best* solution, and includes all the epochs in which the fixed solution was not accepted and the float was kept along with the epochs that were successfully fixed (e.g. full blue dot series in Figure 8 for each trial). These statistics are shown in Table IV. In Table IV, the median performance with UWB remains under 10cm, which in the case of not including UWB is now greater than meter-level performance. Furthermore, over 50%

TABLE IV
STATISTICS OF BASELINE ESTIMATION PERFORMANCE USING OVERALL SOLUTION (BOTH FIXED AND NON-FIXED EPOCHS).

| 750 Trials | with UWB | without UWB |
|---|---|---|
| **Median Overall $3D_{RSS}$ (cm)** | 7.73 | 168.31 |
| **Mean Overall $3D_{RSS}$ (m)** | 42.83 | 110.59 |
| **% of Trials with Overall $3D_{RSS} <= 10cm$** | 54.00 | 1.60 |
| **% of Trials with Overall $3D_{RSS} <= 50cm$** | 67.60 | 16.40 |
| **% of Trials with Overall $3D_{RSS} <= 1m$** | 70.40 | 35.33 |

of trials have an overall $3D_{RSS}$ of less than or equal to 10 cm, whereas this is less than 2% without UWB, and 70% of flights are less than one-meter while this is only 35% without UWB.

Finally, we can gain insight on the baseline estimation performance improvement that is offered by incorporating the UWB ranging measurements by looking at the overall cumulative distribution function of the $3D_{RSS}$ estimation error of the 750 trials. In Figure 9, the impact of peer-to-peer range measurements becomes clear. In particular, the CDF

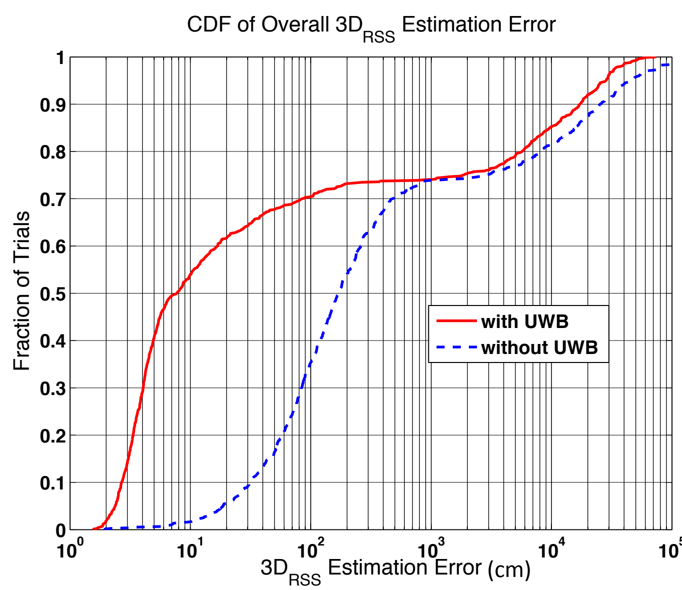


Fig. 9. Cumulative distribution of the $3D_{RSS}$ estimation error over the 750 Monte Carlo simulation trials, where the estimation error is evaluated over all the epochs of each flight (i.e. irrespective of being successfully fixed).

of $3D_{RSS}$ is much steeper when UWB measurements are included, indicating better performance despite the challenging simulated conditions.

## VI. CONCLUSION

This article considered the incorporation of UWB peer-to-peer range measurements to assist DGPS/INS dynamic baseline estimation of UAVs flying in close formation. A novel fusion formulation was developed and evaluated within a simulation environment. The benefit of incorporating UWB peer-to-peer ranges when confronted with scenarios that typically degrade DGPS performance including poor satellite geometry and an increase level of phase breaks was characterized with the use of a Monte Carlo analysis. Whenever phase ambiguities are correctly integer resolved, there is no need for incorporating UWB ranges, however in the face of DGPS challenged conditions, which regularly occur on small UAVs with fast dynamics, there is a clear benefit of incorporating this additional navigation aid. In particular, the ability to fix integer phase ambiguities correctly is significantly increased and the float solution is much more accurate when UWB peer-to-peer ranging is incorporated in the relative navigation filter. In the future, we plan to offer experimental evaluation of the presented fusion approach using the *Phastball* UAVs while flying in formation. In addition, it will be important and interesting to consider the robustness of the algorithm performance to independent sensor reliability concerns (e.g. latent transmission of carrier phase observable, unreliable UWB ranging, etc.), we plan to pursue this in a future investigation.

## ACKNOWLEDGMENT

This work was supported in part by the NASA WV EPSCoR and WV Research Challenge Fund seed grant Program, and NASA Grant #NNX14AF55A.

## REFERENCES

[1] P. A. Rosen, S. Hensley, K. Wheeler, G. Sadowy, T. Miller, S. Shaffer, R. Muellerschoen, C. Jones, H. Zebker, and S. Madsen, "Uavsar: a new nasa airborne sar system for science and technology research," in *Radar, 2006 IEEE Conference on*. IEEE, 2006, pp. 8–pp.

[2] G. Campa, M. L. Fravolini, A. Ficola, M. R. Napolitano, B. Seanor, and M. G. Perhinschi, "Autonomous aerial refueling for uavs using a combined gps-machine vision guidance," in *AIAA Guidance, Navigation, and Control Conference and Exhibit, Providence, RI*, 2004.

[3] T. J. Larrabee, "Wind and wake sensing with uav formation flight: System development and flight testing," 2013.

[4] T. Larrabee, H. Chao, M. Rhudy, Y. Gu, and M. R. Napolitano, "Wind field estimation in uav formation flight," in *American Control Conference (ACC), 2014*. IEEE, 2014, pp. 5408–5413.

[5] C. Rice, Y. Gu, H. Chao, T. Larrabee, S. Gururajan, M. Napolitano, T. Mandal, and M. Rhudy, "Control performance analysis for autonomous close formation flight experiments," in *Unmanned Aircraft Systems (ICUAS), 2014 International Conference on*, May 2014, pp. 1175–1180.

[6] W. Williamson, T. Rios, and J. L. Speyer, "Carrier phase differential gps/ins positioning for formation flight," in *American Control Conference, 1999. Proceedings of the 1999*, vol. 5. IEEE, 1999, pp. 3665–3670.

[7] W. R. Williamson, M. F. Abdel-Hafez, I. Rhee, E.-J. Song, J. D. Wolfe, D. F. Chichka, and J. L. Speyer, "An instrumentation system applied to formation flight," *Control Systems Technology, IEEE Transactions on*, vol. 15, no. 1, pp. 75–85, 2007.

[8] X. Wang, N. Cui, and J. Guo, "Ins/visnav/gps relative navigation system for uav," *Aerospace Science and Technology*, vol. 28, no. 1, pp. 242–248, 2013.

[9] G. MacGougan, K. O'Keefe, and R. Klukas, "Tightly-coupled gps/uwb integration," *Journal of Navigation*, vol. 63, no. 01, pp. 1–22, 2010.

[10] E. Broshears, "Ultra-wideband radio aided carrier phase ambiguity resolution in real-time kinematic gps relative positioning," Ph.D. dissertation, Auburn University, 2013.

[11] Time-Domain, "P-410 ultra wideband ranging and communications module," http://www.timedomain.com/datasheets/TD_DS_P410_RCM_FA.pdf, 2014, accessed: 2014-07-12.

[12] K. H. Jones and J. Gross, "Reducing size, weight, and power (swap) of perception systems in small autonomous aerial systems," in *14th AIAA Aviation Technology, Integration, and Operations Conference*. AIAA, 2014.

[13] D. Simon, *Optimal state estimation: Kalman, H infinity, and nonlinear approaches*. John Wiley & Sons, 2006.

[14] M. Rhudy, Y. Gu, J. Gross, S. Gururajan, and M. Napolitano, "Sensitivity and robustness analysis of ekf and ukf design parameters for gps/ins sensor fusion," *AIAA Journal of Aerospace Information Systems*, vol. 10, no. 3, pp. 131–143, 2013.

[15] J. N. Gross, Y. Gu, M. B. Rhudy, S. Gururajan, and M. R. Napolitano, "Flight-test evaluation of sensor fusion algorithms for attitude estimation," *Aerospace and Electronic Systems, IEEE Transactions on*, vol. 48, no. 3, pp. 2128–2139, 2012.

[16] P. Misra and P. Enge, *Global Positioning System: Signals, Measurements and Performance Second Edition*. Lincoln, MA: Ganga-Jamuna Press, 2006.

[17] B. L. Stevens and F. L. Lewis, *Aircraft control and simulation*. John Wiley & Sons, 2003.

[18] Y. E. Bar-Sever, P. M. Kroger, and J. A. Borjesson, "Estimating horizontal gradients of tropospheric path delay with a single gps receiver," *Journal of Geophysical Research: Solid Earth (1978–2012)*, vol. 103, no. B3, pp. 5019–5035, 1998.

[19] G. Blewitt, "Basics of the gps technique: observation equations," *Geodetic applications of GPS*, pp. 10–54, 1997.

[20] E. D. Kaplan and C. J. Hegarty, *Understanding GPS: principles and applications*. Artech house, 2005.

[21] G. Blewitt, "An automatic editing algorithm for gps data," *Geophysical Research Letters*, vol. 17, no. 3, pp. 199–202, 1990.

[22] M. Rothacher, T. Springer, S. Schaer, and G. Beutler, "Processing strategies for regional gps networks," in *Advances in Positioning and Reference Frames*. Springer, 1998, pp. 93–100.

[23] P. J. Teunissen, "The least-squares ambiguity decorrelation adjustment: a method for fast gps integer ambiguity estimation," *Journal of Geodesy*, vol. 70, no. 1-2, pp. 65–82, 1995.

[24] P. Joosten, "The lambda-method: Matlabtm implementation," 2001.

[25] P. J. Teunissen and S. Verhagen, "The gnss ambiguity ratio-test revisited: a better way of using it," *Survey Review*, vol. 41, no. 312, pp. 138–151, 2009.

[26] Y. Gu, J. Gross, F. Barchesky, H. Chao, and M. Napolitano, "Avionic design for a sub-scale fault tolerant flight control test-bed," *Chapter*, vol. 21, pp. 499–522, 2012.

[27] GPSoft, "Satellite navigation toolbox 3.0 user's guide," 2003.

[28] I. Analog Devices, "Tri-axis inertial sensor with magnetometer: Adis16405," http://www.analog.com/static/imported-files/data_sheets/adis16405.pdf, 2009, accessed: 2014-06-16.

[29] A. K. McGrail, *OnBoard Parameter Identification for a Small UAV*. West Virginia University, 2012.

[30] Y. Gu, B. Seanor, G. Campa, M. R. Napolitano, L. Rowe, S. Gururajan, and S. Wan, "Design and flight testing evaluation of formation control laws," *Control Systems Technology, IEEE Transactions on*, vol. 14, no. 6, pp. 1105–1112, 2006.

[31] C. Goad and L. Goodman, "Modified hopfield tropospheric refraction correction model," in *TRANSACTIONS-AMERICAN GEOPHYSICAL UNION*, vol. 55, no. 12. AMER GEOPHYSICAL UNION 2000 FLORIDA AVE NW, WASHINGTON, DC 20009, 1974, pp. 1106–1106.

[32] B. W. Parkinson and J. J. Spilker, *Progress In Astronautics and Aeronautics: Global Positioning System: Theory and Applications*. Aiaa, 1996, vol. 2.

[33] "Igs products," http://www.igs.org/components/prods.html, 2014, accessed: 2014-07-15.

[34] F. J. Barchesky, J. N. Gross, Y. Gu, M. Rhudy, and M. R. Napolitano, "Development of a gps/ins sensor fusion simulation environment using flight data," in *2011 AIAA Modeling and Simulation Technologies Conference, Portland, OR*, 2011.

[35] J. Gross, Y. Gu, and D. B., "Tightly-coupled gps/uwb-ranging for relative navigation during formation flight," in *Proceedings of the 27th International Technical Meeting of the ION Satellite Division, ION GNSS+ 2014*, September 2014, pp. 1698–1708.

**Jason N. Gross** received a Bachelor's of Science in mechanical engineering and a Bachelor's of Science in aerospace engineering in 2007 from West Virginia University(WVU), Morgantown, WV a and a Ph.D. in aerospace engineering in 2011 also from WVU.

From 2011-2014 he was a research technologist in the Near Earth Tracking Applications Group at the Jet Propulsion Laboratory. Since 2014, he has been an assistant professor in the Department of Mechanical and Aerospace Engineering at WVU. His primary research interests include GNSS, data fusion, and unmanned aerial vehicles.

Dr. Gross is currently a member of the American Institute of Aeronautics and Astronautics (AIAA) and the Institute of Navigation (ION).

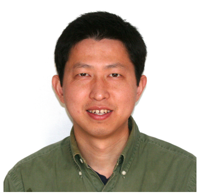

**Yu Gu** earned a B.S degree in Automatic Controls from Shanghai University in 1996, a M.S. degree in Control Engineering from Shanghai Jiaotong University in 1999, and a Ph.D. degree in Aerospace Engineering from West Virginia University in 2004.

From 2004-2012 he was a Research Assistant professor in the department of mechanical and aerospace engineering at West Virginia University. Since 2012, has an assistant professor at WVU.

Dr. Gu is interested in the areas of sensing and control, with applications to robotic systems.

**Matthew B. Rhudy** received a Bachelor's of Science in mechanical engineering in 2008 from The Pennsylvania State University, State College, PA, a Master's of Science in mechanical engineering in 2009 from the University of Pittsburgh, Pittsburgh, PA, and a Doctorate of Philosophy in aerospace engineering in 2013 from West Virginia University, Morgantown, WV.

Since 2013, he has been a Visiting Assistant Professor in the Department of Mechanical Engineering at Lafayette College, Easton, PA. His primary research interests include information fusion, autonomous systems, unmanned aerial vehicles, and instrumentation.

Dr. Rhudy is currently a member of the American Institute of Aeronautics and Astronautics (AIAA).